Near-Wake Investigations of Cylinder and Normal Flat Plate: Effect of Seeding on PIV Measurements

S. Marcocci[1,*], G.P. Romano[2]

1: Dept. of Mechanical and Aerospace Engineering, Sapienza University of Rome, Italy
2: Dept. of Mechanical and Aerospace Engineering, Sapienza University of Rome, Italy
*Corresponding author: mailto:stefano.marcocci@uniroma1.it

Keywords: PIV processing, Near-Wake, Tracers, Bluff bodies, POD, Velocity profiles.

ABSTRACT

Particle Image Velocimetry (PIV) relies on the assumption that tracer particles faithfully follow the fluid. While a small Stokes number (Stk $\ll 1$) is the standard criterion for faithful tracking, it is not sufficient in flows containing organised coherent vortices: particles denser than the fluid are centrifugally expelled from vortex cores and accumulate in strain-dominated regions – a phenomenon known as preferential concentration – which scales with the density ratio ρ_p/ρ_f independently of particle size. This work investigates whether this distinction affects PIV measurements in the near wake of a circular cylinder and a normal flat plate, both of aspect ratio $AR \simeq 6.67$, at Re $= 37500$ and 57300, measured at the off-midspan plane $z/L = 0.25$. Two tracers of widely different density ratio are compared under identical flow conditions: air-filled soap bubbles ($\rho_p/\rho_f \approx 30$) and oil droplets ($\rho_p/\rho_f \approx 800$), both with Stk $\ll 0.01$. The comparison is structured through scalar integral metrics applied to transverse profiles of mean velocity, turbulence intensities and Reynolds shear stress, and through a Proper Orthogonal Decomposition (POD) of the velocity fluctuation fields. In the cylinder wake, the two tracers yield broadly equivalent results, consistent with the absence of compact organised vortices within the measurement domain at this off-midspan location. In the flat plate wake, measurable differences emerge in the POD modal energy distribution, suggesting that preferential concentration becomes relevant where an organised vortex street forms within the field of view. The implications of these findings for the choice of seeding in bluff-body PIV experiments are discussed, together with the limitations of the present dataset.

Nomenclature

$a_k(t)$	Temporal coeff. of mode k [m/s]	$\bar{d}_p$	Mean tracer particle diameter [m]
AR	Aspect ratio L/D or L/H [–]	$\mathcal{E}_{rel}^{(k)}$	Fractional energy of POD mode k [–]
$B_{\tilde{q}}$	Normalised integral bias of q [–]	E_{def}	Relative error on wake deficit [%]
D	Cylinder diameter [m]	H	Flat plate height [m]

I_{def}	Integrated wake deficit [–]
l_B	Recirculation (formation) length [m]
L	Cylinder / flat plate span [m]
$\mathbb{L}$	Characteristic length: D or H [m]
N_u	PIV grid points $N_y \times N_x$ [–]
N_x, N_y	PIV grid dimensions [–]
Re	Reynolds number $U_\infty \mathbb{L}/\nu$ [–]
RMSE	Root Mean Square Error [–]
S_q	Normalisation scale for quantity q
St	Strouhal number $f\mathbb{L}/U_\infty$ [–]
Stk	Stokes number τ_p/τ_f [–]
t_{acq}	Acquisition duration [s]
u, v	Long./transv. velocity [m/s]
$\bar{u}$, $\bar{v}$	Time-avg. velocity components [m/s]
$\overline{u'v'}$	Turbulent shear stress [$\mathrm{m}^2/\mathrm{s}^2$]
U_∞	Freestream velocity [m/s]
x, y, z	Long./transv./spanwise coords [m]
z/L	Normalised spanwise position [–]
ξ, η	Normalised coordinates $x/\mathbb{L}$, $y/\mathbb{L}$ [–]
Δt	Camera exposure time [s]
Δx, Δy	PIV grid spacing [m]
λ_k	k-th POD eigenvalue [$\mathrm{m}^2/\mathrm{s}^2$]
ρ_f	Fluid (air) density [kg/m^3]
$\bar{\rho}_p$	Mean tracer particle density [kg/m^3]
σ_u, σ_v	Std. deviation of (u, v) [m/s]
τ_p	Particle response time $\bar{\rho}_p \bar{d}_p^2/18\mu$ [s]
$\boldsymbol{\psi}_k$	k-th POD spatial mode $\in \mathbb{R}^{2N_u}$ [m/s]

1. Introduction

Particle Image Velocimetry (PIV) reconstructs a flow field from the displacement of tracer particles, and therefore rests on the assumption that the tracers follow the fluid faithfully. While a small Stokes number (Stk $\ll 1$) is the standard criterion for faithful tracking (Raffel et al., 2018), this condition is necessary but not sufficient. Indeed, in flows containing coherent vortices, particles denser than the fluid are centrifugally expelled from vortex cores and accumulate in strain-dominated regions – a phenomenon known as preferential concentration (Maxey, 1987; Squires & Eaton, 1991; Eaton & Fessler, 1994) – whose magnitude scales with ρ_p/ρ_f independently of particle diameter $\bar{d}p$. The present work probes this question by comparing two tracers of widely different density – air-filled soap bubbles ($\rho_p/\rho_f \approx 30$) and oil droplets ($\rho_p/\rho_f \approx 800$), both with Stk $\ll 0.01$ – in the near wake of a circular cylinder and a normal flat plate, both of aspect ratio $AR \simeq 6.67$ and at Reynolds numbers Re $\sim 10^4$. Measurements are taken at the off-midspan plane $z/L = 0.25$, deliberately close to the free end, where – as discussed below – the wake is more strongly influenced by the three-dimensional motions induced by the tip vortices than it is near the midspan.

At the present Re $\sim 10^4$, the cylinder wake lies in the TrSL3 regime, in which transition to turbulence occurs within the separating shear layers and the drag coefficient becomes essentially independent of Reynolds number (Zdravkovich, 1990). The midspan literature of long, nominally two-dimensional cylinders reports a recirculation (vortex-formation) length $l_B \approx 1.3$–$1.5D$ and a shedding Strouhal number St ≈ 0.2 (Perrin et al., 2006; Perret, 2009; Gkiolas et al., 2020; Wang et al., 2018; Capone et al., 2016; Gao et al., 2017; Lysenko et al., 2021; Lysenko, 2025). However, for a cylinder of finite length with a free end, these values are inapplicable at $z/L = 0.25$: tip-vortex downwash from the free end entrains freestream fluid into the wake and elongates the

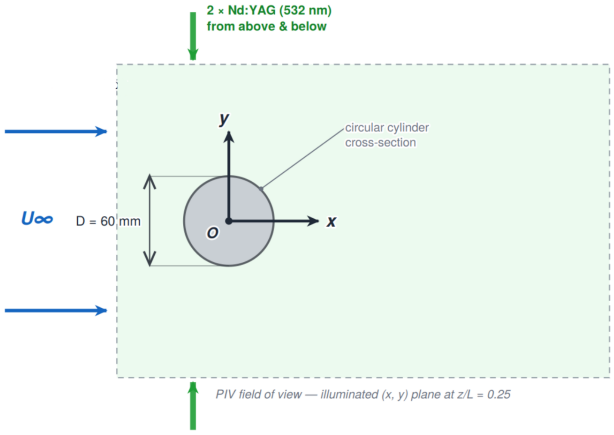
formation region (Park & Lee, 2000; Sumner et al., 2004; Sumner, 2013; Rostamy et al., 2012; Afgan et al., 2007; Azadeh-Ranjbar et al., 2018), suppressing near-wake fluctuations (Williamson, 1996) and pushing the organised vortices far downstream. A direct quantitative comparison with the two-dimensional midspan literature is therefore inapplicable by construction at $z/L = 0.25$; the appropriate references are instead the few studies at similar AR and Re, which report $l_B \approx 3$–$4D$ at comparable AR and Re (Park & Lee, 2000; Rostamy et al., 2012; Afgan et al., 2007).

The normal flat plate literature is considerably sparser: detailed wake studies are predominantly numerical and confined to Re $\ll 10^3$ (Najjar & Balachandar, 1998; Dadmarzi et al., 2011; Jadhav & Narasimhamurthy, 2022), and experiments at intermediate Reynolds numbers typically address modified geometries (Nedić et al., 2013; Cicolin et al., 2024; Ruiz et al., 2009). Nonetheless, a few features relevant to the present work are reported consistently across the available studies. The normal plate sheds an organised von Kármán street at St $\approx$ 0.15–0.16 (Fage & Johansen, 1927; Kiya & Matsumura, 1988; Hemmati et al., 2016) with $l_B \approx 2.5H$ (Hemmati et al., 2016), and a superimposed low-frequency unsteadiness modulates the formation length irregularly (Najjar & Balachandar, 1998; Hemmati et al., 2016; Lisoski, 1993), during which the wake alternates irregularly between a compact, coherent roll-up and a diffuse, downstream-shifted one. Crucially, since separation is fixed at the sharp edges, the organised vortex street forms just behind the model – unlike the cylinder, where the free-end effect pushes it downstream.

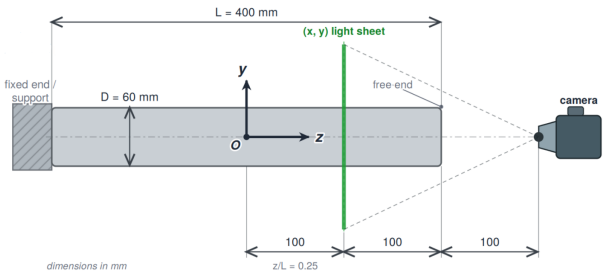
Against this background, the present study has two aims. The primary objective is methodological: to determine whether the seeding choice affects PIV measurements in bluff-body wakes, using integral metrics, transverse profiles, and POD as complementary diagnostics. The unifying expectation is that the two tracers coincide where the FoV (Field of View) contains no organised vortices and diverge where it does. The secondary objective is to provide time-resolved near-wake PIV data for both geometries at $z/L = 0.25$ for finite AR, in a Reynolds-number range that remains sparsely characterised. The remainder of the paper is organised as follows: Section 2 describes the experimental setup; Section 3 presents the results; and Section 4 summarises the findings.

2. Experimental Methodology

Experiments were conducted in the closed-circuit, open-test-section wind tunnel of the Dept. of Mechanical and Aerospace Engineering at Sapienza University of Rome, with circular test section 90 cm $\times$ 120 cm (diameter $\times$ length), contraction ratio 4.35, and turbulence intensity $< 0.5\%$. The models are a PVC circular cylinder ($L \times D = 400 \times 60$ mm) and a plexiglass flat plate ($L \times H \times W = 400 \times 60 \times 10$ mm), sharing the same aspect ratio $AR = L/D = L/H = 6.67$, mounted at the centre of the test section as shown in Fig. 1. Wake measurements were performed using time-resolved 2D-PIV: two continuous Nd:YAG lasers ($\lambda = 532$ nm, sheet thickness $\approx$3 mm) illuminates the vertical (x, y) plane, and a Photron FASTCAM Nova S9 (1024 $\times$ 1024 px, pixel size 20 μm) with a 50 mm



(a) View of the (x, y) plane.



(b) View of the (y, z) plane.

Figure 1. Schematic of the experimental PIV setup for the cylinder; the flat plate setup is identical.

Nikkor lens ($f/1.2$) recorded the images. Measurements were taken at $U_\infty = \{10, 15\}$ m/s (cases V10, V15), corresponding to Re $= \{37500, 57300\}$, with two seeding particles introduced upstream of the contraction: air-filled soap bubbles from the TSI BG-1000 bubble generator, and oil droplets from a Laskin nozzle, whose properties are listed in Table 1. Both tracers have Stk $\ll 0.1$ (Raffel et al., 2018). The four combinations of velocity and tracer type (V10_OIL, V10_SOAP, V15_OIL, V15_SOAP) were measured for each model; camera settings are given in Table 2. PIV analysis was performed using PIVlab with identical settings for all the four PIV cases: three-pass multipass with window deformation, windows 64–32–16 px at 50% overlap, yielding a $N_y \times N_x = 127 \times 127$ vector grid with spacing $\Delta x = \Delta y \simeq 1.3$ mm and a velocity uncertainty of $\approx 1\%\, U_\infty$.

Table 1. Physical and mechanical properties of the PIV tracers.

	OIL	SOAP
$\bar{d}_p$ [μm]	2	15
$\bar{\rho}_p$ [kg/m^3]	920	40
τ_p [μs]	11	27
Stk [$-$]	0.0023	0.0057

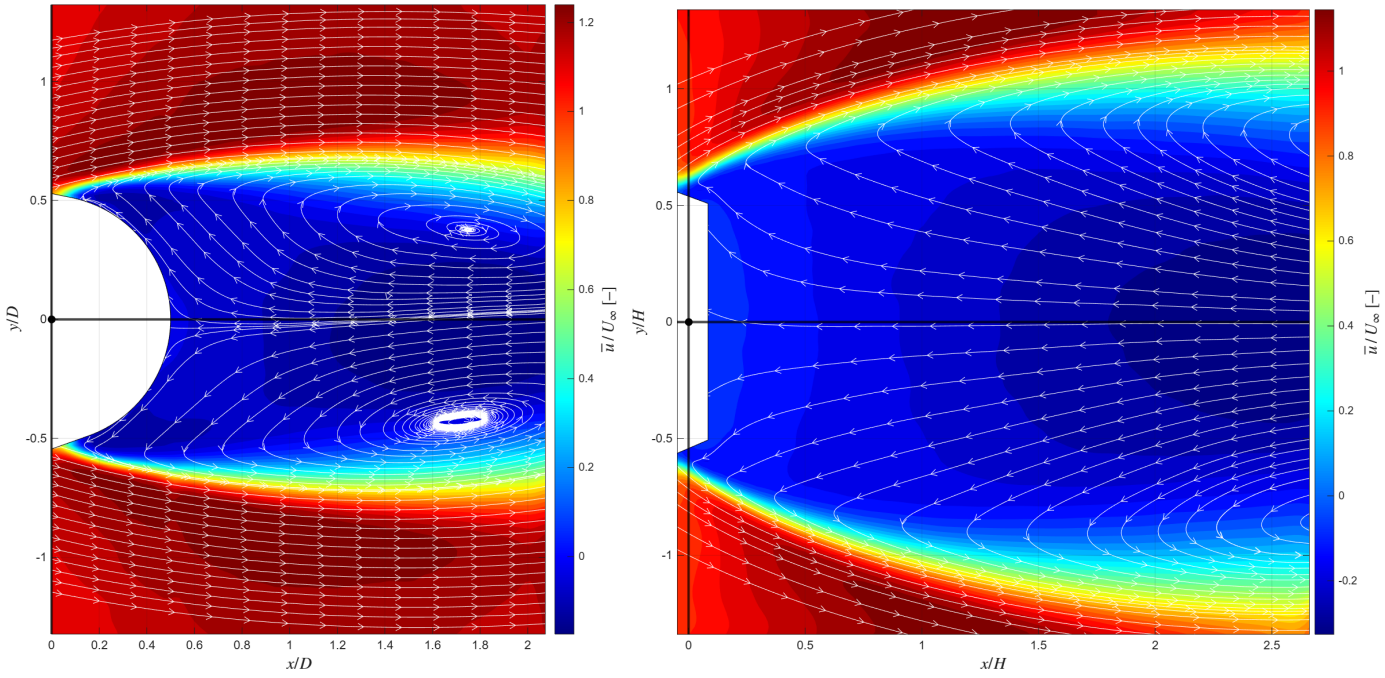
Table 2. Camera settings for the four cylinder and flat plate PIV cases.

PIV CASE	V10_OIL	V10_SOAP	V15_OIL	V15_SOAP
FPS [Hz]	9000	9000	12000	12000
Δt [s]	1/12000	1/12000	1/16000	1/16000
t_{acq} [s]	9.7	9.7	9.7	9.7
Images	87357	87357	116476	116476

3. Results

This section presents the tracer comparison for both models at Re $= 37500$ and Re $= 57300$. Results are structured in three steps: global evaluation via the integral metrics (§ 3.2), local comparison through transverse profiles (§ 3.3), and assessment of the effect on POD decomposition (§ 3.4). All statistics were computed over the full image sets of Table 2, and all transverse profiles shown are resampled to 200 points along y-axis from the original $N_y = 127$ grid points.

3.1. Flow field overview



(a) Cylinder wake.

(b) Flat plate wake.

Figure 2. Streamlines and contour plots of the time-averaged u component for **(a)** cylinder and **(b)** flat plate. For both cases, soap bubbles have been used and the freestream velocity is $U_\infty = 10\,m/s$, corresponding to $Re \simeq 37500$.

The time-averaged velocity vector patterns and the non-dimensional streamwise velocity $\bar{u}/U_\infty$ contours are plotted in Fig. 2 for both models at $Re \simeq 37500$. In the cylinder wake (Fig. 2a), the two counter-rotating recirculation bubbles are centred far downstream, with foci at $(\xi, \eta) \simeq (1.75, \pm 0.4)$ in agreement with the simulations by Afgan et al. (2007) for $AR = 6$ at $Re = 20000$, which place the recirculation centres at $\xi \simeq 2$. For the flat plate (Fig. 2b), the wake is considerably wider, and the recirculation centres lie beyond the Field Of View (FoV), estimated at $\xi \simeq 3$. Unlike the cylinder, the flat-plate recirculation bubble is perfectly symmetric about the y-axis.

3.2. Integral metrics comparison

From these velocity fields, obtained for both the cylinder and the flat plate for each PIV case, we extract the transverse profiles of several physical quantities and compare them by means of the integral metrics, defined as follows. Let $(\xi, \eta) := (x/\mathbb{L}, y/\mathbb{L})$ denote the streamwise and transverse coordinates normalised by the characteristic length $\mathbb{L}$ (D for the cylinder, H for the flat plate). For a generic physical quantity q, the inter-tracer comparison at each streamwise station ξ is quantified through three scalar metrics integrated over the transverse extent $\Delta\eta \in [\eta_{min}, \eta_{max}]$:

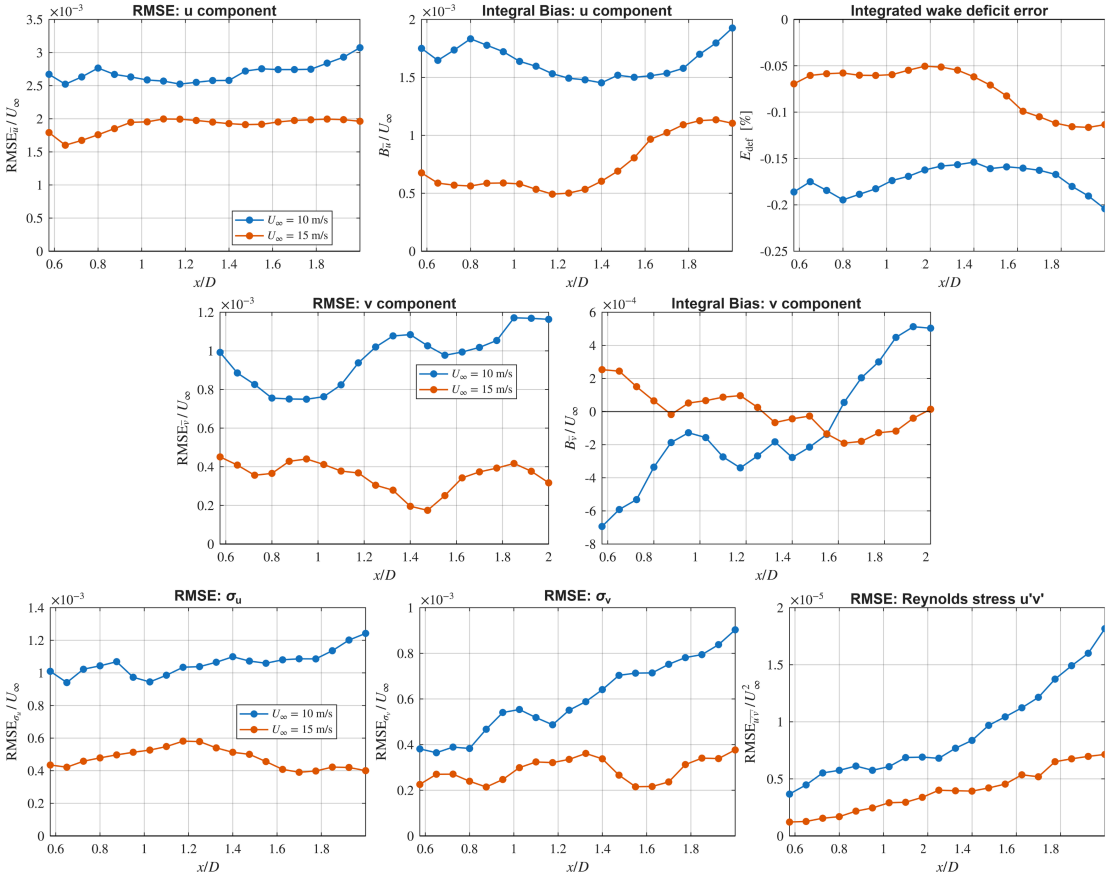


Figure 3. Comparison of eight integral metrics for $U_\infty = 10\,m/s$ (blue lines) and $U_\infty = 15\,m/s$ (orange lines) along 20 stations in $\xi \in [0.6, 2]$ in the cylinder wake. From left to right: $\mathrm{RMSE}_{\tilde{u}}$, $B_{\tilde{u}}$, and E_{def} (row 1); $\mathrm{RMSE}_{\tilde{v}}$ and $B_{\tilde{v}}$ (row 2); $\mathrm{RMSE}_{\tilde{\sigma}_u}$, $\mathrm{RMSE}_{\tilde{\sigma}_v}$, and $\mathrm{RMSE}_{\widetilde{u'v'}}$ (row 3).

$$\mathrm{RMSE}_{\tilde{q}}(\xi) := \sqrt{\frac{1}{\Delta\eta}\int_{\eta_{\min}}^{\eta_{\max}} \left(\frac{q_{\mathrm{soap}} - q_{\mathrm{oil}}}{S_q}\right)^2 \mathrm{d}\eta} \tag{1}$$

$$B_{\tilde{q}}(\xi) := \frac{1}{\Delta\eta}\int_{\eta_{\min}}^{\eta_{\max}} \frac{q_{\mathrm{soap}} - q_{\mathrm{oil}}}{S_q}\,\mathrm{d}\eta \tag{2}$$

$$E_{\mathrm{def}}(\xi) := \left(\frac{I_{\mathrm{def,soap}}(\xi)}{I_{\mathrm{def,oil}}(\xi)} - 1\right) \times 100, \quad I_{\mathrm{def}} := \int_{\eta_{\min}}^{\eta_{\max}} \max\left(1 - \frac{\bar{u}}{U_\infty}, 0\right) \mathrm{d}\eta \tag{3}$$

where $S_q = U_\infty$ for velocities and standard deviations, $S_q = U_\infty^2$ for Reynolds stresses. The RMSE measures the RMS magnitude of the inter-tracer difference; the bias B preserves the sign and detects systematic over- or underestimation; E_{def} quantifies the relative error on the aerodynamic drag inferred from the wake deficit. The quantities q considered are $(\bar{u}, \bar{v}, \sigma_u, \sigma_v, \overline{u'v'})$. Fig. 3 shows eight integral metrics for the cylinder wake. The RMSE values for all quantities are nearly constant along ξ, indicating no downstream divergence between tracers. The bias $B_{\tilde{u}}$ is positive and uniform, so soap systematically overestimates $\bar{u}$ and marginally underestimates drag relative

to oil; $B_{\bar{v}}$ instead varies linearly and changes sign, suggesting a position-dependent response of the two tracers to the evolving wake dynamics. The inter-tracer discrepancy in σ_u is uniform along ξ, while that in σ_v grows approximately linearly, consistent with the increasing cross-stream energy content as the wake widens downstream. Overall, inter-tracer differences in the cylinder wake are systematic rather than random, and consistent across both velocities, but remain within 0.1–0.3% of U_∞ for velocity quantities and a few $\times 10^{-5}\, U_\infty^2$ for turbulent quantities — negligible relative to the flow scale and within PIV measurement uncertainty. A corresponding analysis for the flat plate yields metrics of the same order of magnitude; results are omitted for brevity.

3.3. Local profiles comparison

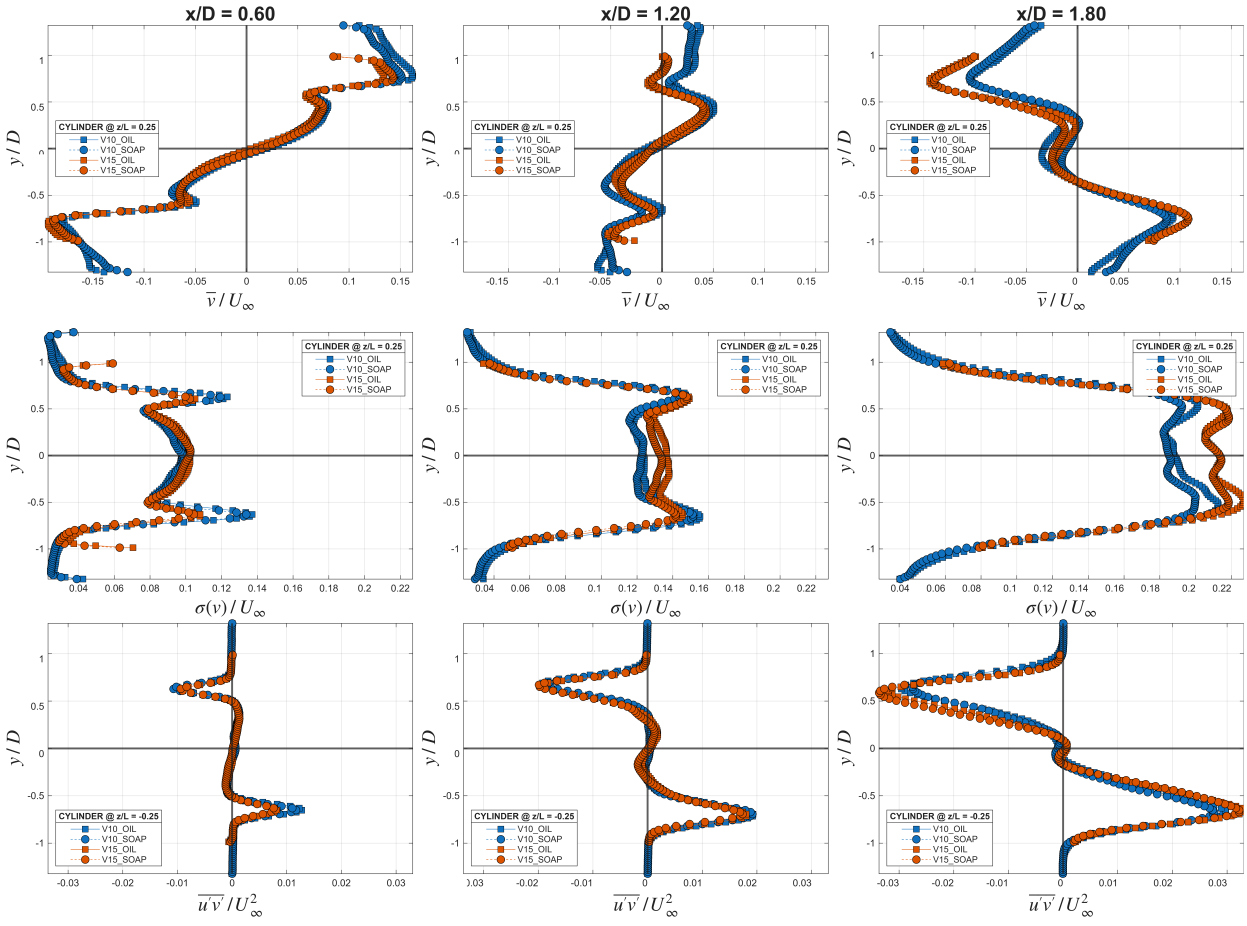


Figure 4. Non-dimensional transverse profiles of $\bar{v}$ (row 1), σ_v (row 2), and $\overline{u'v'}$ (row 3) in the cylinder wake at $z/L = 0.25$, for three streamwise stations $\xi = \{0.6, 1.2, 1.8\}$. Blue and orange symbols correspond to $U_\infty = 10$ and 15 m/s, respectively; circles denote oil droplets and squares soap bubbles.

To provide a more complete description of the differences between soap bubbles and oil droplets, we examine the transverse profiles directly (rather than through their integral differences) for sev-

eral quantities, for both the cylinder and the flat plate. Fig. 4 shows the transverse profiles of $(\bar{v}, \sigma_v, \overline{u'v'})$ for the cylinder at three streamwise stations $\xi = \{0.6, 1.2, 1.8\}$. The $\bar{v}/U_\infty$ profiles display the expected antisymmetric shape, with the lateral velocity diminishing near the foci at $(\xi, \eta) \simeq (1.75, \pm 0.4)$ as ξ increases. The σ_v/U_∞ profiles show the canonical double-lobe structure, strengthening downstream as the shear layers roll up; the $\overline{u'v'}/U_\infty^2$ profiles display the antisymmetric double-peak shape characteristic of bluff-body wakes, with amplitude growing monotonically with ξ, consistent with the trend of $\mathrm{RMSE}_{\overline{u'v'}}$ in Fig. 3. In all panels, soap and oil overlap almost perfectly, confirming the small inter-tracer differences reported in § 3.2. An equivalent agreement is observed for the flat plate, as can be seen from Fig. 5.

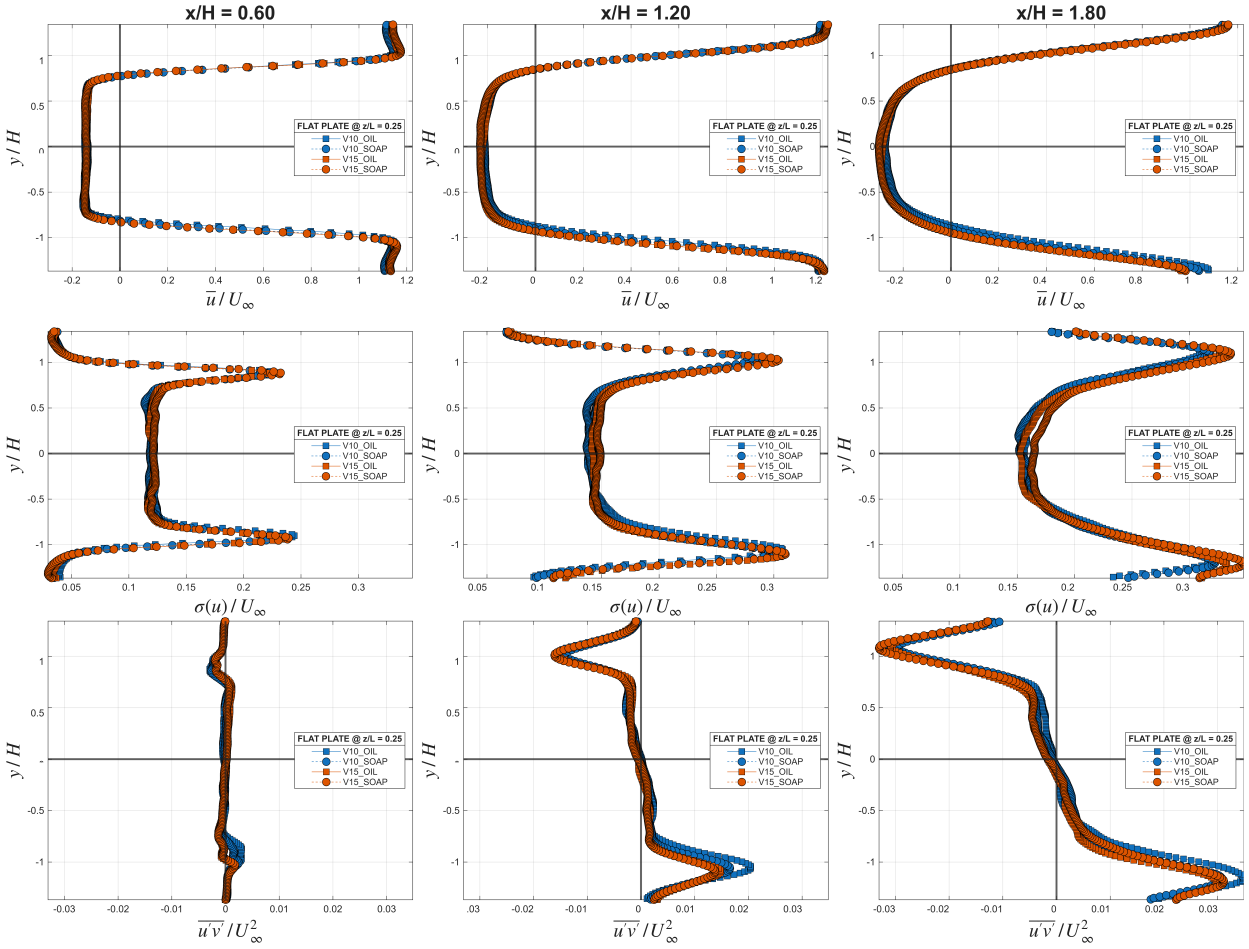


Figure 5. Non-dimensional transverse profiles of $\bar{u}$ (row 1), σ_u (row 2), and $\overline{u'v'}$ (row 3) in the flat plate wake at $z/L = 0.25$, for three streamwise stations $\xi = \{0.6, 1.2, 1.8\}$. Blue and orange symbols correspond to $U_\infty = 10$ and 15 m/s, respectively; circles denote oil droplets and squares soap bubbles.

Since both tracers yield identical transverse profile shapes, neither can be identified as more accurate than the other, and a comparison with the literature is required to assess physical plausibility. The centreline velocity in Fig. 6 confirms $l_B \sim 3.5D$, in agreement with Rostamy et al. (2012) ($AR = 7$, $l_B \sim 3D$ at $z/L = 0.25$), Afgan et al. (2007) ($AR = 6$, $l_B \sim 3.5D$), and Park & Lee (2000)

($AR = 6$, $l_B = 4D$ at midspan). Midspan Pitot profiles corroborate this picture with $l_B \sim 4.5D$ – larger, consistently with the monotonic decrease of l_B toward the free end driven by tip-vortex downwash (Sumner et al., 2004; Sumner, 2013; Azadeh-Ranjbar et al., 2018), and so validating the measurements and confirming that both tracers faithfully reproduce the physical cylinder wake.

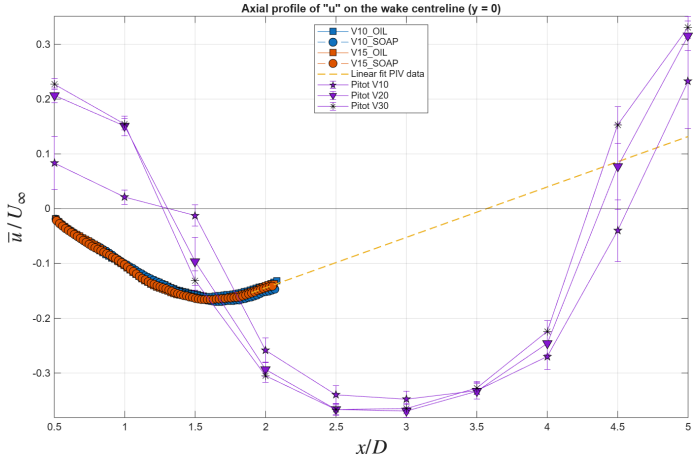


Figure 6. Streamwise centreline velocity $\bar{u}/U_\infty$ profiles for different cases. Blue/orange: PIV cases at $z/L = 0.25$. Yellow: linear extrapolation from $\xi = 1.8$. Purple: midspan Pitot-tube profiles at $U_\infty = \{10, 20, 30\}$ m/s.

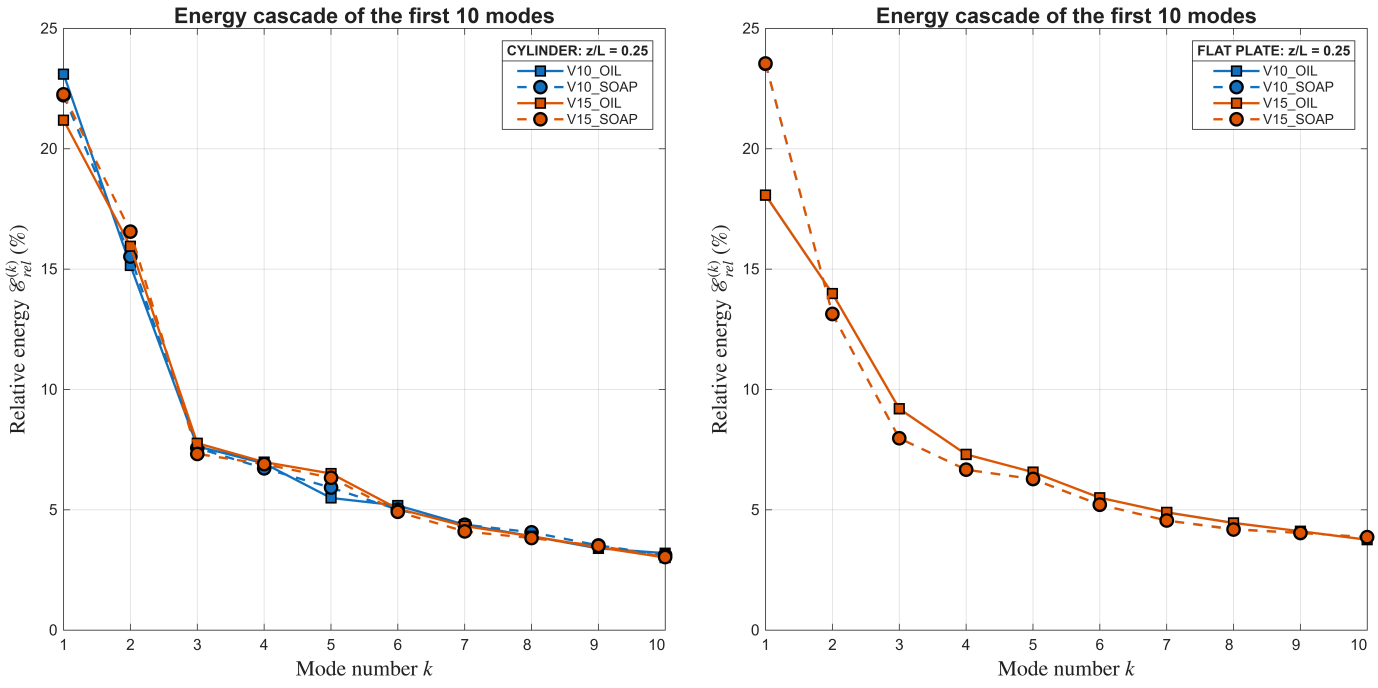
3.4. POD analysis

The profile comparisons of § 3.2 and § 3.3 are pointwise: they detect local inter-tracer differences but cannot reveal whether the two seeders capture the same large-scale flow organisation. A spatially correlated offset – invisible to profile-averaged metrics – could still shift the energy distribution across POD modes. The velocity fluctuation fields are therefore decomposed via the method of snapshots (Sirovich, 1987): the N_s snapshots are assembled into the snapshot matrix $\mathbf{S} \in \mathbb{R}^{2N_u \times N_s}$, with $N_u := N_y \times N_x$, and the spatial modes $\boldsymbol{\psi}_k(\boldsymbol{x})$, temporal coefficients $a_k(t_j)$, and fractional energies $\mathcal{E}_{rel}^{(k)}$ are obtained from the eigenpairs $(\lambda_k, \boldsymbol{\varphi}_k)$ of the temporal correlation matrix $\mathbf{C} := \mathbf{S}^T\mathbf{S}$:

$$\boldsymbol{\psi}_k = \frac{1}{\sqrt{\lambda_k}}\mathbf{S}\,\boldsymbol{\varphi}_k, \qquad a_k(t_j) = \sqrt{\lambda_k}\,\varphi_k(j), \qquad \mathcal{E}_{rel}^{(k)} := \frac{\lambda_k}{\sum_l \lambda_l} \tag{4}$$

where $\lambda_k \geq 0$ is the turbulent kinetic energy captured by mode k, $\boldsymbol{\varphi}_k \in \mathbb{R}^{N_s}$ is the corresponding temporal eigenvector, and $a_k(t_j)$ is the projection of snapshot j (ie. the j-th column of $\mathbf{S}$) onto mode k, encoding how strongly that mode is excited at each time instant. The first 10 modes are computed for each PIV case and compared across tracers in terms of spatial patterns, power spectra of $a_k(t)$, and fractional energy content $\mathcal{E}_{rel}^{(k)}$.

3.4.1. Eigenvalues and energy cascade



(a) Cylinder.

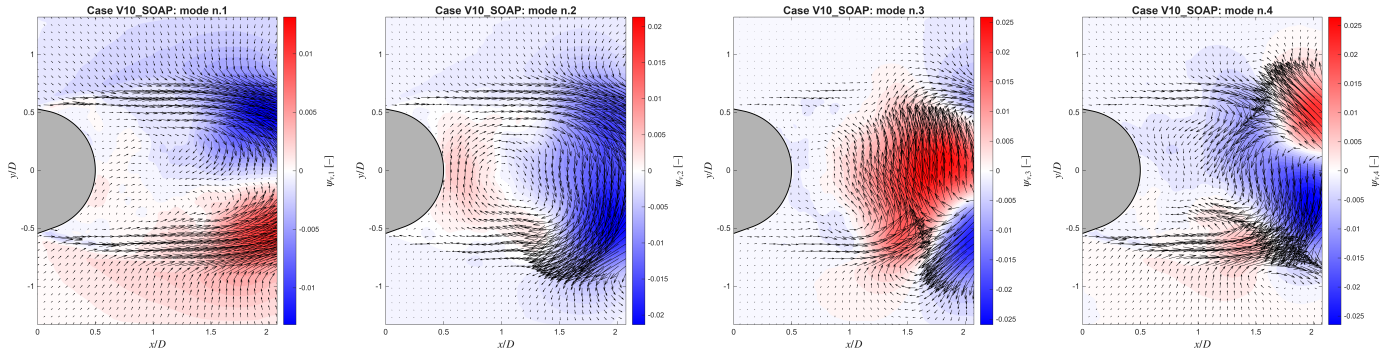
(b) Flat plate.

Figure 7. Relative energy content of the first 10 POD modes for **(a)** the cylinder and **(b)** the flat plate at $z/L = 0.25$.

Fig. 7a shows the relative energy content $\mathcal{E}_{rel}^{(k)}$ of the first 10 POD modes for the cylinder across the four analysed cases. The four curves collapse throughout the entire cascade, with deviations not exceeding $\pm 1\%$, so the modal energy distribution is insensitive to the tracer choice. The energy cascade of the flat plate depicted in Fig. 7b shows that, at fixed tracer, the two velocities yield nearly identical profiles. The inter-tracer comparison, however, reveals a systematic offset absent in the cylinder: soap overestimates $\mathcal{E}_{rel}^{(1)}$ by approximately 5% relative to oil, while underestimating $\mathcal{E}_{rel}^{(k)}$ for $k \geq 2$ by up to 1%, with the discrepancy decreasing with increasing mode number.

3.4.2. Cylinder: analysis of the first 4 POD modes

The spatial structure of the first four POD modes, shown in Fig. 8, reveals the physical content behind this energy ranking. Mode 1 displays the antisymmetric double-lobe pattern of the alternating von Kármán vortex shedding, with two regions of opposite sign symmetric about the cylinder axis. Mode 2 is its quadrature companion, with a single large region of uniform sign spanning the downstream wake and vectors rotating outward from the cylinder base. Together they form the conjugate pair describing the periodic convection of the vortex street. Modes 3 and 4 carry finer spatial structure associated with higher harmonics or shear-layer instabilities.



(a) Mode n.1. (b) Mode n.2 (c) Mode n.3 (d) Mode n.4

Figure 8. Spatial patterns of the first four POD modes of the cylinder at $z/L = 0.25$: V10_SOAP case.

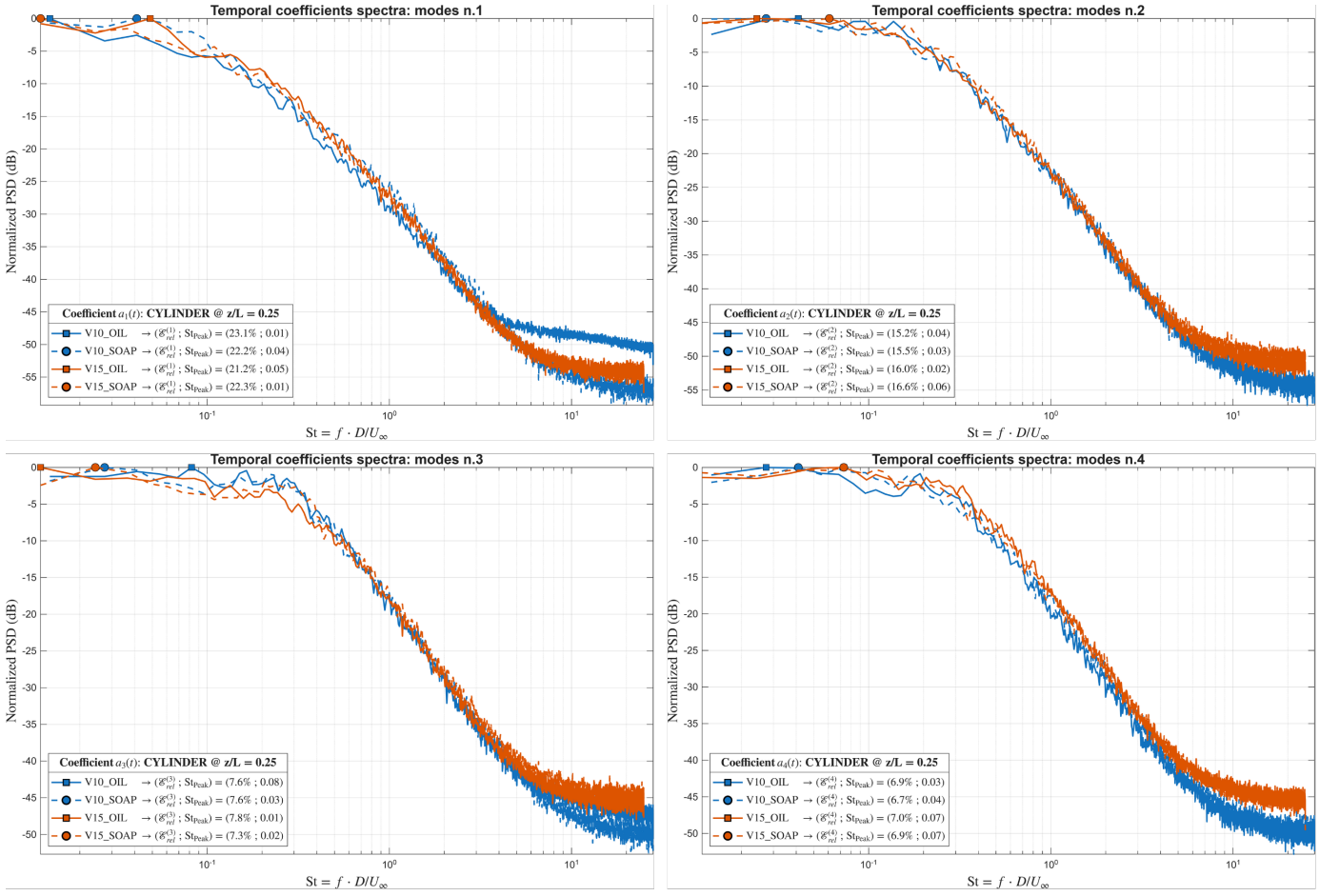


Figure 9. Spectra of the first four coefficients $a_k(t)$ of the cylinder POD modes at $z/L = 0.25$, for all four PIV cases.

Fig. 9 shows the PSD of $a_k(t)$ for the first four POD modes normalised to their maximum value. All spectra exhibit a broadband decay with no identifiable shedding peak, and the dominant Strouhal numbers lie in the range St $\approx$ 0.04–0.08, well below the canonical value of St $\sim$ 0.2 for a 2D cylinder (Wang et al., 2018; Capone et al., 2016). This result may appear at odds with Sumner et al. (2004),

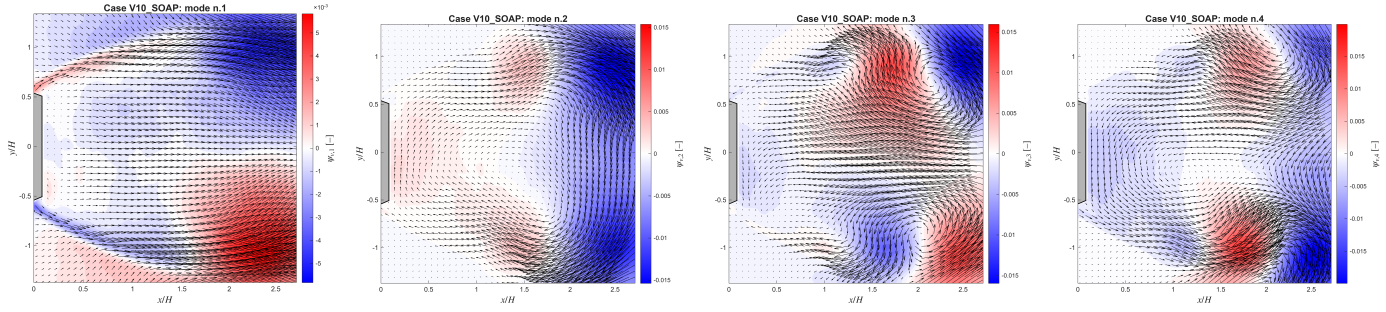
who consistently reports a peak near St $\simeq 0.16$ for cylinders with $AR = 5$–9 at spanwise positions $z/L \in [-0.3, 0.4]$; however, those measurements are taken at $(\xi, \eta) = (3, 1.5)$, well outside the present FoV. Indeed, for the present cylinder $l_B \sim 3.5D$ (Fig. 6) and the recirculation vortices' foci are located at $\xi \simeq 1.8$ (Fig. 2), so the entire FoV falls within the vortex formation region. Here the shear layers are still rolling up and the von Kármán vortex street has not yet reached a stable, periodic organisation, which explains both the absence of a spectral peak and the relatively low energy content of the first two modes: $(\mathcal{E}_{rel}^{(1)}, \mathcal{E}_{rel}^{(2)}) \approx (22\%, 16\%)$ are considerably lower than the $(\mathcal{E}_{rel}^{(1)}, \mathcal{E}_{rel}^{(2)}) \approx (30-40\%, 20-30\%)$ reported in Wang et al. (2018) and in Perrin et al. (2006) for flows where the von Kármán shedding dominates. Indeed, in the formation region, energy is distributed across many modes and a broad range of frequencies, rather than concentrated in a single periodic process, and this seems to be our case.

Across all four modes, the PSD curves collapse well over the entire frequency range; therefore, in this FoV the choice of seeding particles does not affect the POD description of the cylinder wake at any level of the modal analysis.

3.4.3. Flat plate: analysis of the first 4 POD modes

The flat plate results, shown in Figs. 10 and 11, differ notably from those of the cylinder and require a more careful interpretation of the modal structure.

Although the spatial modes of Fig. 10 appear at first glance analogous to the cylinder, the temporal spectra of Fig. 11 reveal a fundamentally different structure. Modes 2 and 4 share a clear spectral peak at the same Strouhal number: they form the true von Kármán conjugate pair, consistent with the expected shedding frequency for a normal flat plate $\mathrm{St}_{\mathrm{peak}} \sim 0.15$–$0.16$ (Hemmati et al., 2016; Fage & Johansen, 1927; Kiya & Matsumura, 1988). Unlike the cylinder – where the entire FoV lies within the formation region – the flat plate has fixed separation points at the sharp leading edges, which force the shear layers to roll up at shorter streamwise distances; coherent shedding therefore develops within the available FoV. Mode 1, by contrast, shows a flat, featureless spec-



(a) Mode n.1. (b) Mode n.2 (c) Mode n.3 (d) Mode n.4

Figure 10. Spatial patterns of the first four POD modes of the flat plate at $z/L = 0.25$: V10_SOAP case.

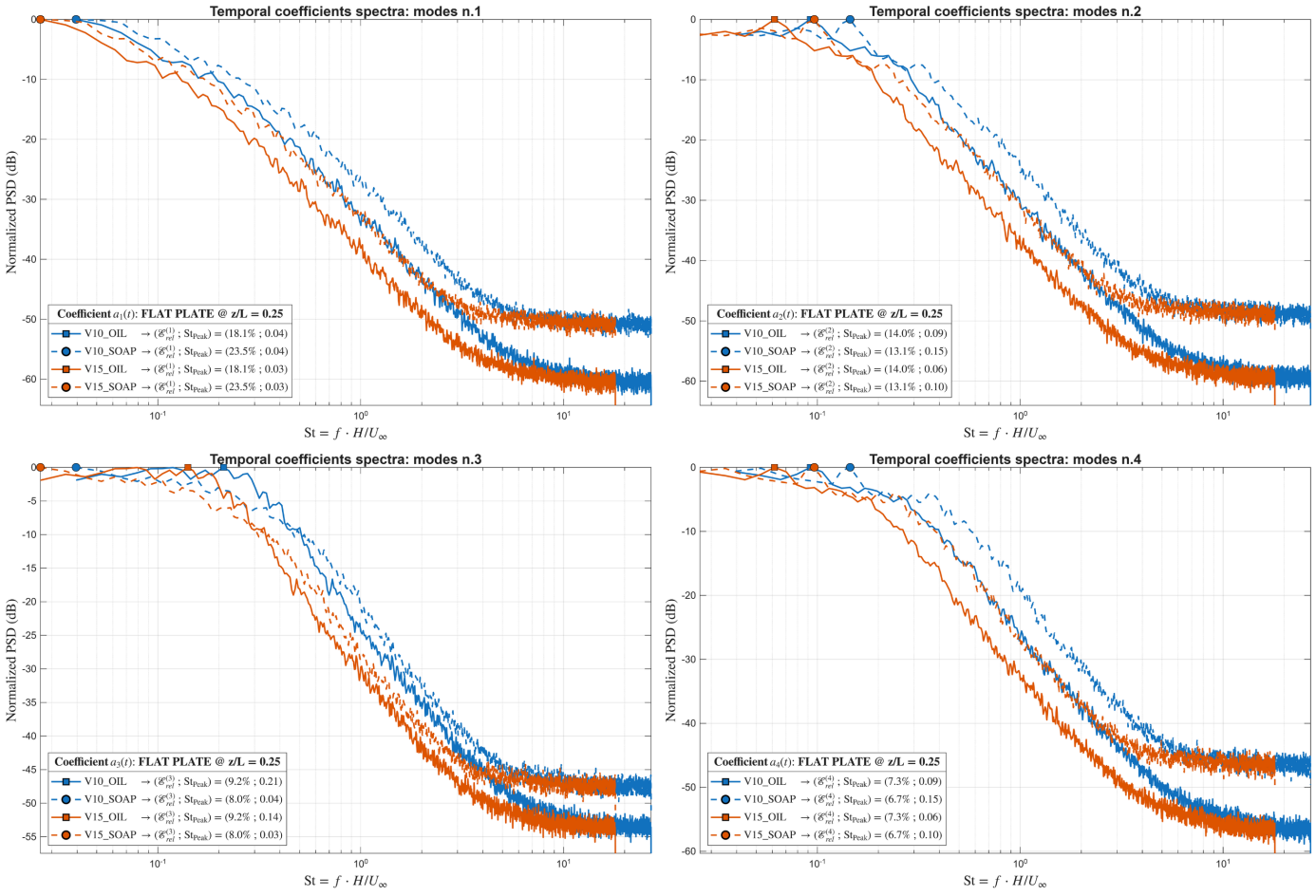


Figure 11. Spectra of the first four coefficients $a_k(t)$ of the flat plate POD modes at $z/L = 0.25$, for all four PIV cases.

trum, capturing the low-frequency unsteadiness documented by Najjar & Balachandar (1998): the flat plate wake alternates irregularly between a high-drag regime of compact, coherent shedding ($l_B \sim 1.7H$) and a low-drag regime of diffuse, delayed roll-up ($l_B \sim 3.1H$), on a timescale roughly ten times the shedding period. This switching produces a broadband spectrum and, because it modulates the entire wake, dominates the POD energy cascade. The mechanism is reported also for $Re = 12500$ (Lisoski, 1993), suggesting it extends to the Reynolds numbers of the present study.

The spectra of modes 2 and 4 reveal an important tracer effect: the dominant Strouhal numbers differ substantially between tracers – $\mathrm{St}_{\mathrm{peak}} \approx 0.09$ for V10_OIL against ≈ 0.15 for V10_SOAP on mode 2, with the same ratio reproduced on mode 4 and at V15 (but with a lower $\mathrm{St}_{\mathrm{peak}}$). Comparison with the literature identifies oil as the source of the discrepancy: Fage & Johansen (1927), Kiya & Matsumura (1988), and Hemmati et al. (2016) consistently report $\mathrm{St}_{\mathrm{peak}} \sim 0.15$–$0.16$ for a normal flat plate, and the soap-measured value is in close agreement with all three references. The oil-measured value falls well below any published data – and notably below even the low-drag-regime bound of Najjar & Balachandar (1998), who report $\mathrm{St} \in [0.143, 0.167]$ across their high- and low-drag regimes, a range within which the soap-measured $\mathrm{St}_{\mathrm{peak}} \approx 0.15$ falls squarely. A plau-

sible physical explanation lies in the different density ratios of the two tracers with respect to air. Despite both tracers having Stk $\ll 0.01$, this is primarily a consequence of their small diameters ($d_p \approx 2\,\mu$m for oil, $d_p \approx 15\,\mu$m for soap), which keep $\tau_p = \rho_p d_p^2/(18\mu)$ low regardless of density. The centrifugal drift within a vortex, however, scales as $(\rho_p - \rho_f)\,\omega^2 r$ and depends on ρ_p/ρ_f independently of particle size – on which Stk does depend. Oil droplets ($\rho_p/\rho_f \approx 800$) are therefore centrifugally expelled from vortex cores and undergo preferential concentration in low-vorticity regions (Maxey, 1987; Squires & Eaton, 1991; Eaton & Fessler, 1994), undersampling the periodic dynamics and reporting a depressed shedding frequency. Soap bubbles ($\rho_p/\rho_f \approx 30$) experience smaller centrifugal drift relative to oil droplets, and therefore capture the dominant shedding more faithfully, even if both share Stk $\ll 0.01$. This frequency error is the most physically significant difference between the two tracers found in this study.

4. Conclusions

Soap bubbles and oil droplets have been compared as PIV tracers in the near wakes of a finite circular cylinder and a normal flat plate both with $AR \simeq 6.67$, at $Re \simeq 37500$ and 57300, and at $z/L = 0.25$ through integral metrics, transverse profiles analysis, and POD decomposition.

At the level of time-averaged and turbulent statistics, the two tracers are practically equivalent for both geometries: inter-tracer discrepancies amount to at most 0.1–0.3% of U_∞ for velocity quantities – within the PIV measurement uncertainty – and a few $\times 10^{-5}\,U_\infty^2$ for turbulent stresses, and transverse profiles are virtually indistinguishable. The formation length $l_B \sim 3.5D$ estimated from the cylinder data agrees well with published results (Rostamy et al., 2012; Afgan et al., 2007; Park & Lee, 2000), validating the physical plausibility of the profiles at $z/L = 0.25$.

The POD analysis reveals where the equivalence breaks down. The cylinder FoV ($\xi \lesssim 2$) lies entirely within the formation region ($l_B \sim 3.5D$), where both tracers observe the same disorganised fluctuations and the modal energy distribution is insensitive to the tracer choice. The flat plate FoV ($\xi \lesssim 2.5$), by contrast, captures organised von Kármán shedding: oil droplets yield $\mathrm{St}_{\mathrm{peak}} \approx 0.09$ while soap bubbles yield $\mathrm{St}_{\mathrm{peak}} \approx 0.15$, in agreement with the literature (Fage & Johansen, 1927; Kiya & Matsumura, 1988; Hemmati et al., 2016; Najjar & Balachandar, 1998). The oil bias is attributed to preferential concentration (Maxey, 1987; Squires & Eaton, 1991; Eaton & Fessler, 1994): despite Stk $\ll 0.01$ for both tracers, oil droplets ($\rho_p/\rho_f \approx 800$) are centrifugally expelled from vortex cores because the centrifugal drift scales as $(\rho_p - \rho_f)\,\omega^2 r$, independently of d_p – on which Stk does depend. Soap bubbles, having $\rho_p/\rho_f \approx 30$, sample the flow more faithfully.

The absence of inter-tracer differences in the cylinder likely reflects the limited FoV rather than a genuine insensitivity: since preferential concentration depends only on ρ_p/ρ_f and the presence of compact vortices, an analogous discrepancy would be expected beyond l_B. More generally, tracer fidelity depends on whether organised vortical structures are present in the measurement

domain: when they are, density-driven preferential concentration causes tracers with $\rho_p/\rho_f \gg 1$ to undersample the dominant dynamics, while tracers with $\rho_p/\rho_f \sim 1$ provide a more accurate representation. Soap bubbles are therefore not merely an acceptable substitute for oil droplets: in flows with organised shedding, they are the superior tracer.

Several open questions warrant further investigation: whether the same inter-tracer discrepancy emerges in the organised cylinder wake beyond l_B; the origin of the systematic inter-velocity offset in the integral metrics and in the POD spectra; and whether the tracer sensitivity observed here extends to other flows containing compact, coherent vortices.

References

Afgan, I., Moulinec, C., Prosser, R., & Laurence, D. (2007). Large eddy simulation of turbulent flow for wall mounted cantilever cylinders of aspect ratio 6 and 10. *International Journal of Heat and Fluid Flow*, *28*, 561-574. doi: 10.1016/j.ijheatfluidflow.2007.04.014

Azadeh-Ranjbar, V., Elvin, N., & Andreopoulos, Y. (2018). Vortex-induced vibration of finite-length circular cylinders with spanwise free-ends: Broadening the lock-in envelope. *Physics of Fluids*, *30*. doi: 10.1063/1.5042774

Capone, A., Klein, C., Di Felice, F., & Miozzi, M. (2016). Phenomenology of a flow around a circular cylinder at sub-critical and critical reynolds numbers. *Physics of Fluids*, *28*. doi: 10.1063/1.4954655

Cicolin, M. M., Chellini, S., Usherwood, B., Ganapathisubramani, B., & Castro, I. P. (2024). Vortex shedding behind porous flat plates normal to the flow. *Journal of Fluid Mechanics*, *985*, A40. doi: 10.1017/jfm.2024.300

Dadmarzi, F. H., Narasimhamurthy, V. D., Andersson, H. I., & Pettersen, B. (2011). The turbulent wake behind side-by-side plates. *Journal of Physics: Conference Series*, *318*, 062010. doi: 10.1088/1742-6596/318/6/062010

Eaton, J. K., & Fessler, J. R. (1994). Preferential concentration of particles by turbulence. *International Journal of Multiphase Flow*, *20*, 169–209. doi: 10.1016/0301-9322(94)90072-8

Fage, A., & Johansen, F. C. (1927). On the flow of air behind an inclined flat plate of infinite span. *Proceedings of the Royal Society of London. Series A, Containing Papers of a Mathematical and Physical Character*, *116*, 170-197. doi: 10.1098/rspa.1927.0130

Gao, D.-L., Chen, W.-L., Li, H., & Hu, H. (2017). Flow around a circular cylinder with slit. *Experimental Thermal and Fluid Science*, *82*, 287-301. doi: 10.1016/j.expthermflusci.2016.11.025

Gkiolas, D., Kapiris, P., & Mathioulakis, D. (2020). Experimental study of the near wake of a circular cylinder and its detached shear layers. *Experimental Thermal and Fluid Science*, *113*, 110040. doi: 10.1016/j.expthermflusci.2020.110040

Hemmati, A., Wood, D. H., & Martinuzzi, R. J. (2016). Characteristics of distinct flow regimes in the wake of an infinite span normal thin flat plate. *International Journal of Heat and Fluid Flow*, *62*, 423-436. doi: 10.1016/j.ijheatfluidflow.2016.09.001

Jadhav, P., & Narasimhamurthy, V. D. (2022). Characteristics of wake turbulence generated by a normal flat plate. *International Journal of Fluid Mechanics Research*, *49*, 81-93. doi: 10.1615/InterJFluidMechRes.2022043389

Kiya, M., & Matsumura, M. (1988). Incoherent turbulence structure in the near wake of a normal plate. *Journal of Fluid Mechanics*, *190*, 343-356. doi: 10.1017/S002211208800134X

Lisoski, D. (1993). *Nominally two-dimensional flow about a normal flat plate* (Unpublished doctoral dissertation). California Institute of Technology, Pasadena, California.

Lysenko, D. A. (2025). Large-eddy simulation of the flow past a circular cylinder at re = 130,000: Effects of numerical platforms and single- and double-precision arithmetic. *Fluids*, *10*, 4. doi: 10.3390/fluids10010004

Lysenko, D. A., Donskov, M., & Ertesvåg, I. (2021). Large-eddy simulations of the flow over a semi-circular cylinder at re = 50000. *Computers & Fluids*, *228*, 105054. doi: 10.1016/j.compfluid.2021.105054

Maxey, M. R. (1987). The gravitational settling of aerosol particles in homogeneous turbulence and random flow fields. *Journal of Fluid Mechanics*, *174*, 441–465. doi: 10.1017/S0022112087000193

Najjar, F. M., & Balachandar, S. (1998). Low-frequency unsteadiness in the wake of a normal flat plate. *Journal of Fluid Mechanics*, *370*, 101-147. doi: 10.1017/S0022112098002110

Nedić, J., Ganapathisubramani, B., & Vassilicos, J. C. (2013). Drag and near wake characteristics of flat plates normal to the flow with fractal edge geometries. *Fluid Dynamics Research*, *45*, 061406. doi: 10.1088/0169-5983/45/6/061406

Park, C.-W., & Lee, S.-J. (2000). Free end effects on the near wake flow structure behind a finite circular cylinder. *Journal of Wind Engineering and Industrial Aerodynamics*, *88*, 231-246. doi: 10.1016/S0167-6105(00)00051-9

Perret, L. (2009). Piv investigation of the shear layer vortices in the near wake of a circular cylinder. *Experiments in Fluids*, *47*, 789-800. doi: 10.1007/s00348-009-0665-y

Perrin, R., Braza, M., Cid, E., Cazin, S., Moradei, F., Barthet, A., … Hoarau, Y. (2006). Near-wake turbulence properties in the high reynolds number incompressible flow around a circular cylinder measured by two- and three-component piv. *Flow, Turbulence and Combustion*, *77*, 185-204. doi: 10.1007/s10494-006-9043-5

Raffel, M., Willert, C. E., Scarano, F., Kähler, C. J., Wereley, S. T., & Kompenhans, J. (2018). *Particle image velocimetry - a practical guide* (3rd ed.). Springer. doi: 10.1007/978-3-319-68852-7

Rostamy, N., Sumner, D., Bergstrom, D. J., & Bugg, J. D. (2012). Local flow field of a surface-mounted finite circular cylinder. *Journal of Fluids and Structures*, *34*, 105-122. doi: 10.1016/j.jfluidstructs.2012.04.014

Ruiz, T., Sicot, C., Brizzi, L. E., Laumonier, J., Borée, J., & Gervais, Y. (2009). Unsteady near wake of a flat disk normal to a wall. *Experiments in Fluids*, *47*, 637-653. doi: 10.1007/s00348-009-0702-x

Sirovich, L. (1987). Turbulence and the dynamics of coherent structures - part i: Coherent structures. *Quarterly of Applied Mathematics*, *45*, 561-571. doi: 10.1090/qam/910462

Squires, K. D., & Eaton, J. K. (1991). Preferential concentration of particles by turbulence. *Physics of Fluids A*, *3*(5), 1169–1178. doi: 10.1063/1.858045

Sumner, D. (2013). Flow above the free end of a surface-mounted finite-height circular cylinder: A review. *Journal of Fluids and Structures*, *43*, 41-63. doi: 10.1016/j.jfluidstructs.2013.08.007

Sumner, D., Heseltine, J. L., & Dansereau, O. J. P. (2004). Wake structure of a finite circular cylinder of small aspect ratio. *Experiments in Fluids*, *37*, 720-730. doi: 10.1007/s00348-004-0862-7

Wang, S., Chen, Y., & Liu, Y. Z. (2018). Measurement of unsteady flow structures in a low-speed wind tunnel using continuous wave laser-based tr-piv: near wake behind a circular cylinder. *Journal of Visualization*, *21*, 73-93. doi: 10.1007/s12650-017-0445-3

Williamson, C. H. K. (1996). Vortex dynamics in the cylinder wake. *Annual Review of Fluid Mechanics*, *28*, 477-539. doi: 10.1146/annurev.fl.28.010196.002401

Zdravkovich, M. M. (1990). Conceptual overview of laminar and turbulent flows past smooth and rough circular cylinders. *Journal of Wind Engineering and Industrial Aerodynamics*, *33*, 53-62. doi: 10.1016/0167-6105(90)90020-D